Ultra Low Dissipation Silicon Nanowire Resonator Arrays for Scanning Probe Applications

by

Andrew Jordan

A thesis
presented to the University of Waterloo
in fulfillment of the
thesis requirement for the degree of
Master of Science
in
Physics

Waterloo, Ontario, Canada, 2019

Author's Declaration

I hereby declare that I am the sole author of this thesis. This is a true copy of the thesis, including any required final revisions, as accepted by my examiners.

I understand that my thesis may be made electronically available to the public.

Abstract

This work describes the fabrication and characterization of silicon nanowire oscillators for use in ultra-high sensitivity force detection. These structures are optimized for use as scanning probes by fabricating them at the edge of a chip, allowing for easy optical displacement detection. Two sets of nanowire samples are described, with mean diameters of 132 nm and 77 nm. The characterization of the mechanical properties of the nanowire, such as quality factor and resonant frequency, is done by optical interferometry. The thermomechanical noise-limited force sensitivity of these nanowires is recorded across a range of temperatures and reaches as low as 500 ± 20 $\mathrm{zN}/\sqrt{\mathrm{Hz}}$ at 4.2 K.

Acknowledgements

I would like to thank my supervisor Dr. Raffi Budakian for his support, guidance, and his ability to always have time for his students.

I would also like to thank Dr. Ben Yager and Dr. Pardis Sahafi for sharing their knowledge with respect to the fabrication of these devices. Without their support this project would have been completely overwhelming.

I would like to thank all of the members of our group: Bill Rose for performing the low temperature measurements of the nanowires presented in this work and for several of the plots presented in the measurements and results sections, Michele Piscitelli for her fabrication expertise, and Sahand Tabatabaei for his support and help with some theoretical concepts.

I would also like to thank the staff of the University of Waterloo's Quantum-Nano Fabrication and Characterization Facility, in particular Nathan Nelson-Fitzpatrick, Sandra Gibson, Greg Holloway, and Rodello Salandanan for their advice and expertise.

Thanks is also due to Stefan Heinemann for the TEM images.

Table of Contents

List of Figures

List of Tables

Chapter 1

Introduction

1.1 Scanning Probe Microscopy

Scanning probe microscopy (SPM) is a highly versatile family of techniques used to probe a wide variety of forces and interactions ranging from electromagnetic forces [1, 2] to spin [3, 4] and mass [5, 6] detection. The underlying concept is the investigation of a region of interest by moving a data-acquiring probe across the region to form an image. This concept was first put into practice with the invention of the scanning-tunneling microscope (STM) [7] and atomic force microscope (AFM) [8]. These techniques revolutionized the study of nanoscale structures by introducing a method of imaging surface features with sub-nanometer precision.

Today, the most well known type of SPM is AFM. In AFM, a highly sensitive microscopic cantilever is scanned over a surface and a measurement of its deflection due to a number of forces such as electrical [9], magnetic, or chemical interactions [10, 11] is detected. The cantilever is rastered over the surface and the deflection data is used to construct a topographical image of the surface with extremely high resolution, often in the sub-nanometer regime [8].

The central component of AFM and SPM in general is the probe itself. The push to detect ever-smaller forces has required significant innovation in probe design to keep up with the demand for ever-increasing force sensitivity. In recent years, many novel structures have been proposed and implemented as ultra-sensitive sensors such as carbon nanotubes [12], graphene membranes [13], and semiconductor nanowires [14].

While SPM and AFM are powerful analytical tools, they are not without their limitations. These techniques are limited to probing surfaces and surface interactions and are very limited in their ability to image three-dimensional structures.

1.2 Nanowires as Scanning Probes

Nanowires (NWs) are a class of structures characterized by their diameter on the scale of tens to hundreds of nanometers, and a length typically on the order of microns. These structures are typically composed of semiconductor materials such as Si or III-V materials such as InP or GaAs [14]. Although some top-down techniques (e.g. chemical etching [15]) have been utilized for NW fabrication, most commonly, bottom-up techniques such as chemical vapor deposition (CVD) through the vapor-liquid-solid (VLS) mechanism[16], aerotaxy [17], and molecular beam epitaxy [18] are used. Semiconductor NWs have found a home in a wide range of applications such as logic gates[19], solar cells [20], and as nanoscale lasers[21].

The nature of scanning probes imposes several constraints on the device used for sensing, namely that the sensor must be able to be located near a surface, and its motion must be detectable with a high degree of accuracy. This places strict constraints on the size and shape of the sensor; sensors should be made as small as possible to maximize their sensitivity to small forces, and should be singly-clamped (ie. have one free-standing end). NWs have been shown to possess several qualities that make them ideal sensors for SPM. By the nature of their methods of fabrication, NWs are naturally free standing structures and their dimensions and single-crystal structure cause them to have extremely high force sensitivities and low mechanical dissipations.

NWs have only relatively recently been investigated for SPM applications. Several unique and interesting concepts have been explored using NW sensors such as force-detected magnetic resonance imaging of nuclear spins [22, 23], electromagnetic forces [24, 25], and optomechanical forces [26].

The currently envisioned use of the NWs described in this work is as ultra-sensitive cantilevers for magnetic resonance force microscopy (MRFM). MRFM is a technique wherein the force exerted on nuclear or electron spins by a magnetic field gradient is coupled to the motion of a cantilever[27]. The force is driven at the resonance frequency of the cantilever, and its displacement is detected and used to construct a 3D image of the sample. This technique has been proposed for the imaging of complex biomolecules such as proteins or virus particles [27]. While previous work has demonstrated the feasibility if this technique using nanowire cantilevers [22, 23], the NW sensors described here offer a number of significant advantages over the NWs used previously. NWs presented in previous work were randomly located on their substrate chip, making their detection via optical interferometry reliant on locating a wire near the edge of the sample, NWs in this work are patterned within 10 μm of the chip edge. NWs fabricated for this work display significantly improved force sensing capability due to both their dimensions and high quality.

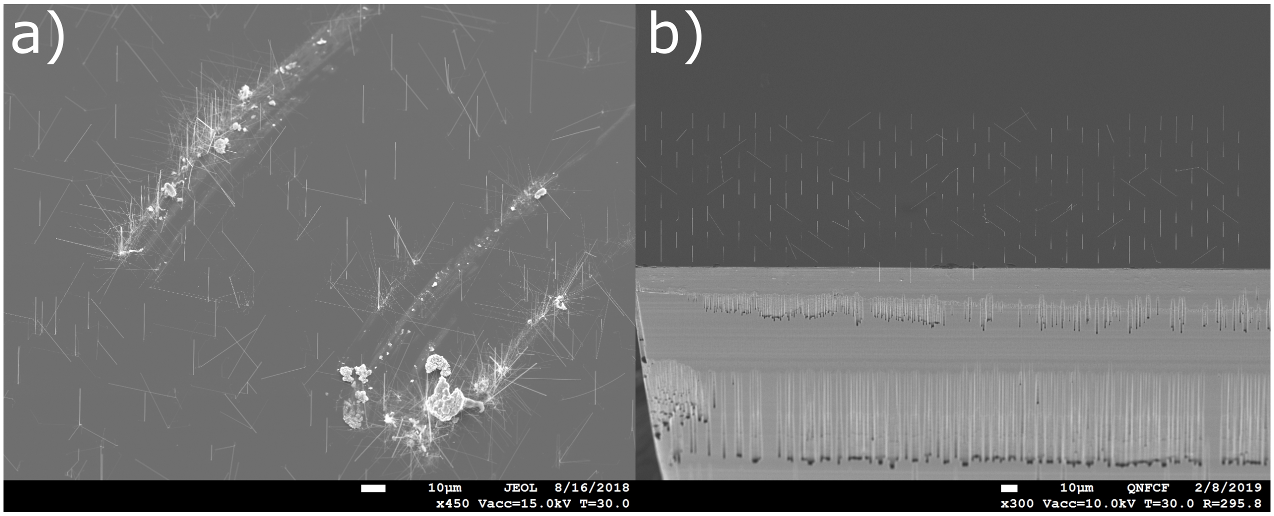

Figure 1.1: a) SEM image of randomly located NWs produced by the dropcast technique (Section 3.2.1) b) SEM image of patterned NW arrays at the edge of a Si chip.

Chapter 2

Background

2.1 Desired Characteristics

To explore the use of SiNWs as ultra-sensitive force sensors, it is important to understand the properties that make them ideally suited for this task. The force sensitivity of a cantilever is limited by its intrinsic mechanical dissipation Γ given by [14]

$$\Gamma = \frac{k}{\omega Q}. \tag{2.1}$$

Where k is the spring constant, ω is the cantilever's resonance frequency, and Q is the quality factor, a dimensionless quantity which is defined as the ratio of energy stored and the energy loss per cycle. Dissipation can arise from a range of sources such as loss due to the coupling to the support structure, lattice defects, and thermoelastic dissipation [28]. For small scale Si structures such as cantilevers or NWs the dissipation is dominated by surface effects caused in part by the presence of a native oxide layer that forms in an air atmosphere [29]. Modeling the nanowire as a singly-clamped cylindrical beam, Euler-Bernoulli beam theory provides the following expressions for k and ω in terms of the dimensions of the NW [30]:

$$k = \left(\frac{3\pi}{4}\right)\left(\frac{R^4}{L^3}\right)E, \tag{2.2}$$

$$\omega = \left(\frac{1.875^2}{2}\right)\left(\frac{R}{L^2}\right)\sqrt{\frac{E}{\rho}}, \tag{2.3}$$

where E is the Young's modulus (168.9 GPa for (111) Si) of the cantilever material, and ρ is the mass density. To examine what properties minimize the mechanical dissipation, we express Γ as

$$\Gamma = 1.34\left(\frac{R^3}{LQ}\right)\sqrt{E\rho}. \tag{2.4}$$

The smallest detectable force using a cantilever of this type is limited by its thermomechanical noise, which is minimized by minimizing the dissipation of the NW. The spectral density of the force fluctuations is given by [28]

$$S_F = 4k_b T\Gamma, \tag{2.5}$$

where k_B is the Boltzmann constant and T is the temperature of the NW. From equation 2.5, to achieve the highest possible force sensitivity, it is necessary to minimize the mechanical dissipation. These expressions make it clear that a cantilever with low mechanical dissipation should be a long, thin structure, with a high Q, and made of a material with small $E\rho$.

NWs are typically fabricated from semiconductor materials, either Si or III-IV materials such as InP [31] or GaAs [24]. Compared to III-V materials Si has a significantly lower density, 2.32 $\mathrm{g/cm^3}$, than that of GaAs (5.32 $\mathrm{g/cm^3}$) or InP (4.81 $\mathrm{g/cm^3}$). The Young's modulus of SiNWs in the range of diameters examined in this work has been shown to not vary significantly from the bulk value[32] and is comparable with that of InP NWs [33].

2.2 VLS Growth

As described in section 1.2, a breadth of fabrication techniques exist for producing NWs. Among these, the VLS mechanism is the most common, owing to its applicability to a large range of semiconductor materials and the relative simplicity of its implementation. NWs in this work were grown by chemical vapor deposition (CVD) using the VLS mechanism. The VLS mechanism was first discussed by R. Wagner and W. Ellis [16] in 1964. This mechanism allows for single crystal growth by adsorption of material from a vapor phase onto a solid surface. This process is mediated by a catalyst particle, typically an alloy of the deposited material and a metal. In the case of this work, a liquid Au-Si alloy particle on a Si substrate is exposed to a silane (SiH_4) flow. Silane cracks at the vapor-solid interface in the following reaction [34] with the Si being dissolved into the liquid alloy droplet (Figure 2.1).

$$\mathrm{SiH_4 \rightarrow Si + 2H_2} \tag{2.6}$$

As Si is added to the liquid alloy droplet, the internal concentration of Si exceeds the equilibrium concentration (determined by the temperature, Figure 2.5) causing the droplet to become supersaturated. Si atoms precipitate out of this supersaturated volume by crystallizing at the solid-liquid phase boundary at the base of the droplet. This deposition forms a single atomic layer of Si aligned to the crystal beneath it and displaces the catalyst droplet upwards.

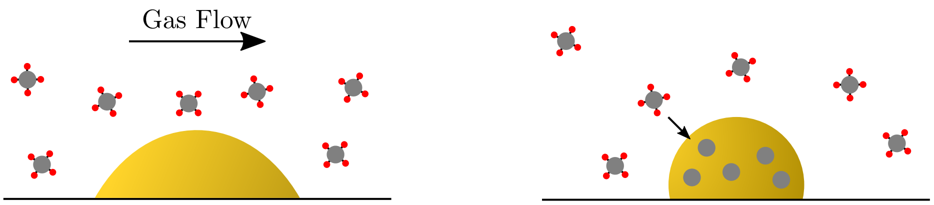

Au-Si droplet is
exposed to SiH$_4$ flow

SiH$_4$ cracks at
liquid-vapor interface

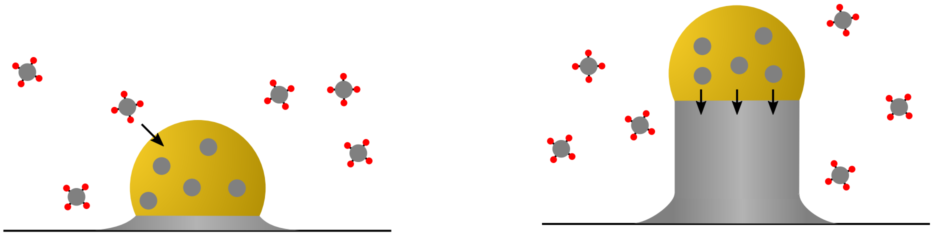

Droplet becomes supersaturated
Si is deposited at liquid-solid interface

Deposition continues
Au-Si droplet remains at tip

Figure 2.1: VLS growth process steps.

When a layer is deposited it causes a change in the contact angle β disturbing the balance of surface tensions holding the droplet at the NW tip (Figure 2.2). This results in a net upwards force on that droplet causing it to move upwards as the NW grows [35]. The forces acting on the droplet originate from the surface tension of the droplet (σ_l), and at the liquid-solid interface (σ_{ls}) .

During the entire growth process, the horizontal component of the force is balanced around the triple phase line, (i.e. $\sigma_l \cos(\beta) = \sigma_{ls}$) resulting in no net horizontal force and restricting the motion of the Au-Si particle to being along the axis of the NW. When a new layer of Si is deposited, there must be a net force upwards on the droplet in order for it to return to its original position relative to the tip of the solid Si section of the NW. If such a force is present, the growth is considered to be stable [36]. For the net force on the droplet to be upwards, $\sigma_{ls} + \sigma_l \sin(\beta) > \sigma_s$. From these two expressions we find that the condition for stable growth is [35]

$$\sin(\beta) - \cos(\beta) > \frac{\sigma_s}{\sigma_l}. \tag{2.7}$$

The maximum value of $\sin(\beta) - \cos(\beta)$ is $\sqrt{2}$ when $\beta = 135°$, therefore for growth to be stable, the catalyst used must have a surface tension that fulfills $\sigma_l > \sigma_s/\sqrt{2}$. This is known as the Nebol'sin stability criterion[37]. Using this criterion it is possible to identify which materials are suitable catalysts keeping in mind that they must also form a liquid eutectic with Si at or below the growth temperature. For the Au-Si system examined in this work, $\sigma_l = 0.9$ J/m^2 and $\sigma_s = 1.2$ J/m^2. [37] This fulfills the stability criterion making Au a suitable catalyst material for SiNW growth. Given this criterion other suitable catalyst materials can be identified. In addition to Au, Ag and Cu have suitable surface tensions for stable SiNW growth [37] and have also been successfully used [38, 39].

Since the deposition of the Si is epitaxial, the direction of growth is determined by the crystal structure and orientation of the substrate. In this work a [111] Si substrate is chosen due to the main direction of growth being normal to the plane of the substrate [40]. With this choice of substrate, three other growth directions are also possible, corresponding to the other {111} directions: $[\bar{1}11]$, $[1\bar{1}1]$, and $[11\bar{1}]$ (Figure 2.4) separated by 120°. One can select the

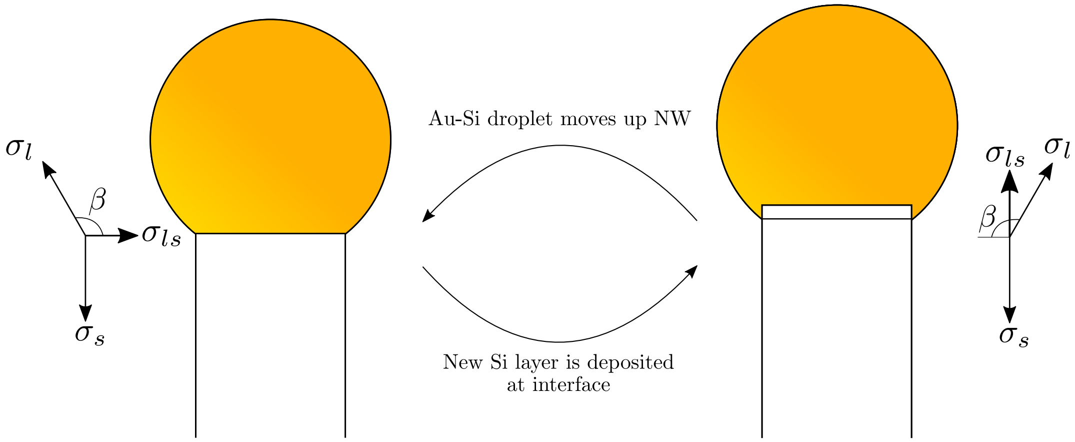

Figure 2.2: Si layer deposition process with force diagrams [36].

desired growth direction by adjusting the temperature at which the growth takes place [41].

It is also possible for the growth direction to change during growth in a process referred to as kinking. When this occurs, NWs transition from growth along the vertical [111] direction to one of the other six possible directions (Figure 2.3). This typically occurs close to the base of the NW but can in principle occur anywhere along the length. It has been shown that kinking is less likely of occur at lower SiH_4 partial pressures and at higher temperatures[41]. Since the yield of vertical NWs is temperature dependent and improves at lower temperatures, we select a growth temperature of 550°C to achieve a balance between these two effects. When the Au catalyst particle is first deposited on the Si surface, (see Section 3.2.1), the deposited material consists of several crystal grains and is composed of pure Au. During an anneal the sample is heated to 400°C under am Ar flow. This is above the Au-Si eutectic temperature (363°C) [42] causing the Au to form a liquid alloy with the Si from the substrate. The relative amounts of Au and Si are the droplet is strongly temperature dependent as shown in Figure 2.5. The liquid alloy droplet wets the Si surface forming a stronger bond between the droplet and the substrate. It was found that this annealing step significantly improved the yield of vertical SiNWs (Section 3.3).

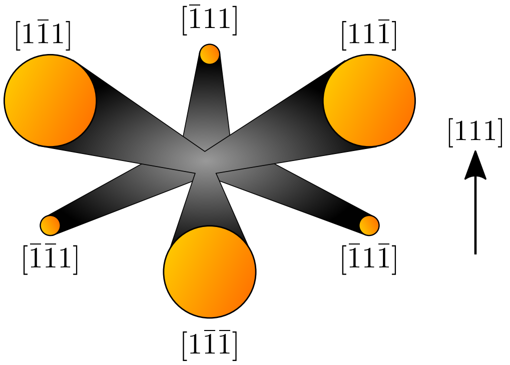

Figure 2.3: {111} growth directions relative to the vertical [111] direction (arrow). Growth can initiate in one of the four upwards directions and kinking causes a switch to another growth direction. [41]

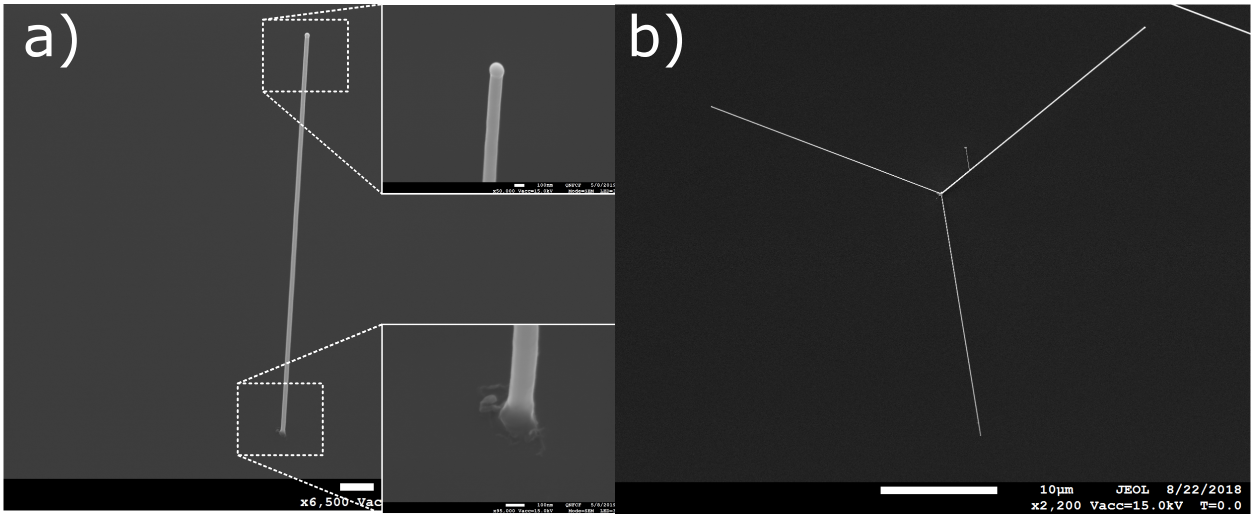

Figure 2.4: a) SEM image of a single vertical SiNW (shown at a 30° tilt angle from vertical). Insets show the base and tip of the NW. Top inset shows the Au catalyst particle at the NW tip. b) SEM image of non-vertical growth directions (Top down view).

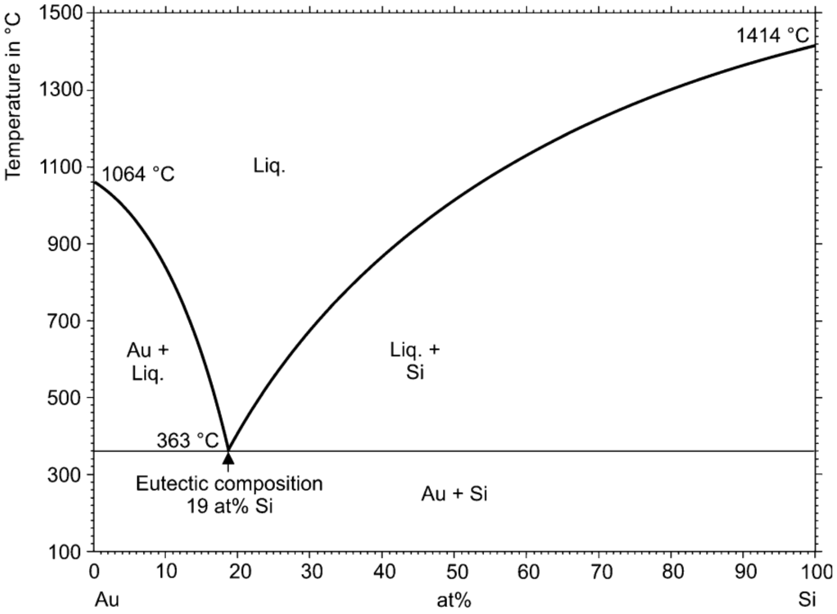

Figure 2.5: Au/Si Eutectic phase diagram [43].

2.3 NW Diameter Prediction

As discussed in Section 2.1, the dimensions of grown SiNWs are key to their implementation as high-sensitivity force transducers. In this section I describe our method of ensuring that our method of predicting the final dimensions of our SiNWs matches the actual dimensions as measured using SEM. While prediction and control over the NW length is straightforward since the growth rate is largely independent of NW diameter[44] and is roughly linear with growth time, predicting the diameter of a NW from the shape of the deposited catalyst particle is less simple.

For a given volume of Au deposited, one can estimate the diameter of a SiNW grown from that Au catalyst particle by [36]

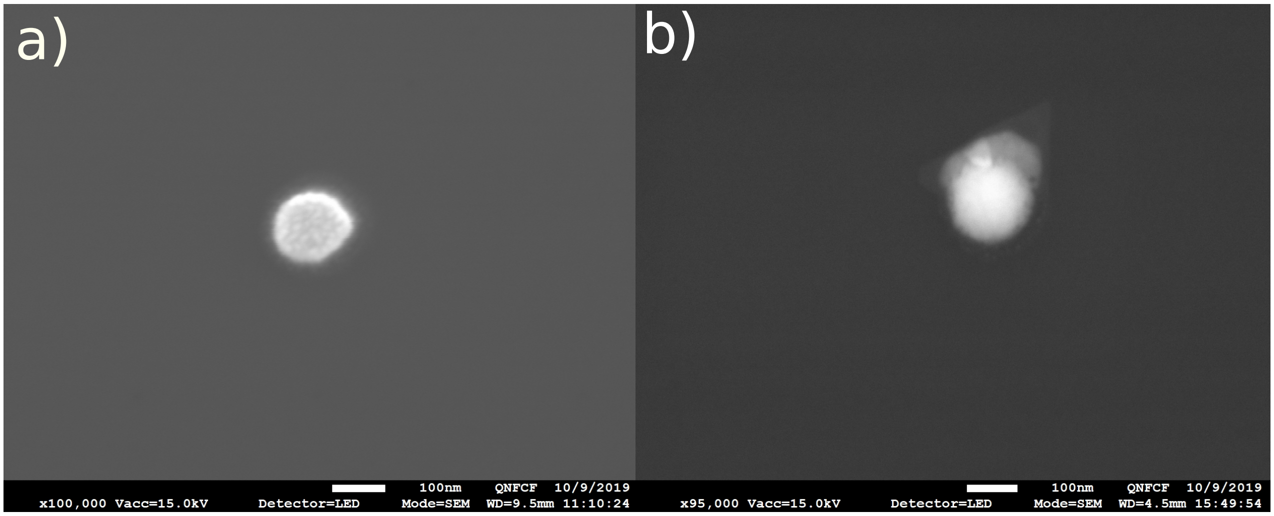

Figure 2.6: SEM image of a single Au catalyst particle a) before annealing and b) after annealing.

$$d = \frac{1}{2}\left(\frac{3V}{\pi}\right)^{1/3} \frac{(1+\cos(\beta))^{1/2}}{(1-\cos(\beta))^{1/6}(2+\cos(\beta))^{1/3}}, \tag{2.8}$$

where V is the volume of the catalyst particle, and β is the angle between the solid-liquid plane and the edge of the liquid catalyst (shown in Figure 2.7) which is often referred to as the contact angle. We estimate Au before annealing to be a cylindrical volume with diameter equal to the diameter of the area exposed during the EBL step and height equal to the thickness of Au deposited (See section 3.2.1). The angle β is determined by the interplay of surface energies between the liquid-solid, solid-vapor, and vapor-liquid interfaces during growth as described by Young's equation [34].

$$\gamma_{SV} - \gamma_{LS} - \gamma_{LV}\cos(\beta) + \frac{\tau}{r} = 0 \tag{2.9}$$

Where the γs are the surface energies of the solid-vapor, liquid-solid, and liquid-vapor interfaces, r is the radius of the droplet, and τ is the surface tension. The surface tension term plays a significant role when the diameter of the droplet is small, but its contribution to the free energy can be neglected at diameters above 12 nm [45].

In other work, values of γ are determined by examining the contact angle of droplets wetting the substrate surface [34] so it is reasonable to assume that one could determine the angle β using values from literature. However, due to the high sensitivity of these values to their environment, it is impractical to calculate β directly from Young's equation. Instead, β is measured directly from TEM images of NWs post-growth.

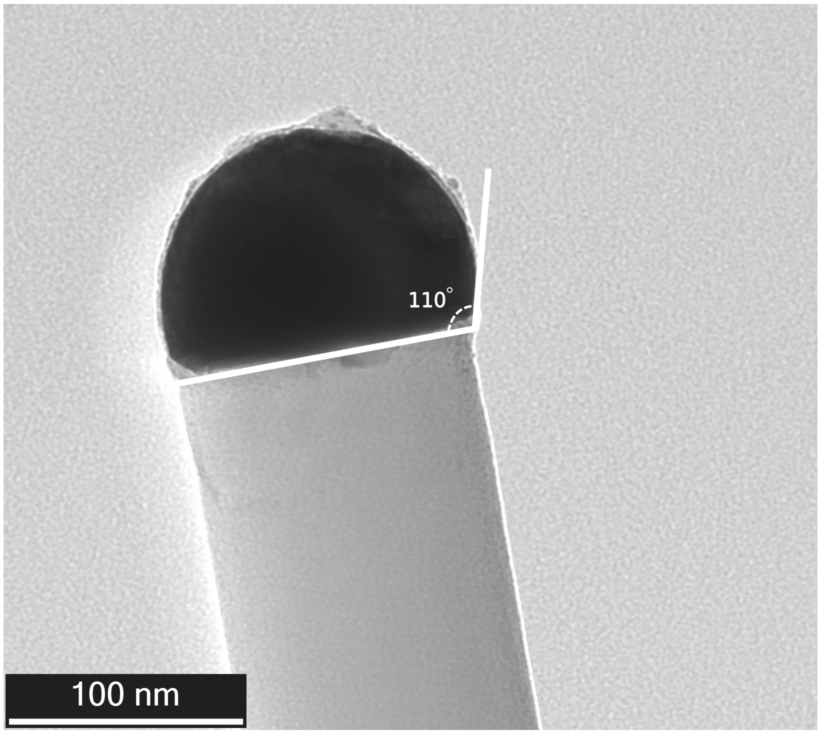

Figure 2.7: TEM image of a NW tip showing the contact angle β.

It is somewhat reasonable to expect this method of determining β to have some inaccuracy due to the change in concentration of Si in the catalyst particle during growth compared to the concentration after growth. Looking at the phase diagram for the Au-Si binary alloy (Figure 2.5), we see that the concentration if Si is 19% at the eutectic temperature and 23% at the growth temperature (550°C). This difference of 4 atomic % Si is not expected to significantly change the volume of the catalyst particle making the measurement of β from the post-growth TEM images a reasonable approximation of the true angle during growth.

Pre-anneal ⌀ (nm)	Post-anneal ⌀ (nm)	Predicted ⌀ (nm)	Measured ⌀ (nm)
84±2	82 ± 4	81	84± 2
110 ± 1	108± 4	97	97±4
132 ± 1	134 ± 7	109	110± 3
147 ± 1	146± 9	117	121± 5

Table 2.1: Comparison of predicted and measured NW diameters

Using TEM images of three SiNWs, we record an average β of 110°. Au volumes were calculated using the mean value of the diameters of 20 catalyst particles after deposition for each diameter (Figure 2.6. The diameters of the grown NWs were shown to match well to the expected diameter, demonstrating our ability to accurately control the dimensions of our NWs.

Chapter 3

Sample Fabrication

The goal of the sample fabrication process is to produce batches of Si chips that are 1 × 1.5 mm in size and have a reasonably large number of high quality, vertical SiNWs located within 10 µm of one of the short edges. Since the motion of the SiNW cantilever is detected optically, the positioning of the NW at the chip edge is key to allowing a detection scheme such as optical interferometry to be able to access an individual NW for study. Fabricating a device with these constraints presents a number of significant challenges. This chapter describes the sample fabrication process and how it addresses the challenges presented by the device requirements. Two diameters of NWs (132 nm and 77 nm) are produced, with slight variations in the fabrication process. With the smaller diameter NWs we expect to see a decrease in the spring constant as well as in the resonance frequency leading to decreased dissipation and therefore a decreased force noise. We do however expect the motion of thinner NWs to be more challenging to detect due to the reduced amount of reflected light.

3.1 Substrate Preparation

SiNWs were grown from 380 μm thick Si [111] substrate. This particular crystal orientation was chosen since growth in the vertical [111] direction requires the lowest energy compared to growth along other crystal directions [40], allowing for a high yield of vertical SiNWs. Beginning with an intrinsic (undoped) silicon wafer, we grow a 1 μm protective SiO_2 layer in a Tystar Tytan 4600 Mini Fourstack Horizontal Furnace. This oxide layer is later etched away, providing a pristine sample surface.

A layer of Shipley 1811 photoresist is applied to the wafer via spincoating (Appendix A). This photoresist layer is used to prevent dust and debris from the dicing process from landing of the surface of the wafer. The wafer is diced into 15×15 mm chips using a Disco DAD3240 dicing saw. We then remove protective photoresist layer by sonicating the chips in PG remover for a period of 15 minutes, and in isopropyl alcohol (IPA) for 5 minutes.

We then clean the diced chips using a RCA clean process [46]. This process is divided into three steps: SC-1, Oxide Etch, and SC-2. The SC-1 step is designed to remove organic contaminants from the chips by immersing them in a bath of 10:2:1 DI Water: 30% Hydrogen Peroxide (H_2O_2): 30% Ammonium Hydroxide (NH_4OH) heated to 70°C. Chips are left in the SC-1 solution for 15 minutes.

Next, the 1 μm thermal oxide layer is removed by etching in 10-1 buffered oxide etchant for 25 minutes. This step leaves behind a pristine sample surface but, along with the SC-1 process, is ineffective at removing metallic contaminants. This step also temporarily passivates the exposed Si surface by hydrogen terminating the dangling bonds that remain after the oxide is removed. The passivation remains for approximately 30 minutes [47].

The SC-2 process consisting of a 10:2:1 solution of DI Water: 30% Hydrogen Peroxide: 30% Hydrochloric Acid (HCl) heated to 70°C. This step is designed to remove metallic contaminants.

Following the cleaning process, we are left with 15×15 mm chips with a pristine, uncontaminated surface. Chips are then dried with a nitrogen flow and stored under vacuum in a vacuum bag.

3.2 Fabrication

3.2.1 Catalyst Particle Patterning

Gold catalyst particles were patterned using two different methods in this work. The first method, drop cast deposition, has the advantage of having a very short and relatively simple fabrication procedure. This allows for quick sample fabrication for testing new growth recipes, or nanowire post-processing procedures at the cost of having no control of nanowire position on the sample chips making it unsuitable for use in creating nanowires for use as probes. The second method, patterning via electron beam lithography (EBL) and chip patterning via deep reactive ion etching (DRIE), provides full control over nanowire position and diameter as well as control over the chip geometry. This method provides nanowires that are suitable for use as scanning probes, but is much more complex and time consuming than the drop cast method. In this work, EBL patterned nanowires were used in almost all nanowire samples grown. All data presented is acquired from EBL patterned NW arrays.

On drop cast samples, Au catalyst particles are deposited by dipping freshly RCA cleaned samples in a solution of 10:2:1 DI Water: 1M HF: Au colloid solution causing the particles to adhere to the sample surface due to Van der Waals forces. The Au solution contains spherical unconjugated Au nanoparticles and can be purchased in a variety of particle sizes to produce different sized NWs.

Processing for catalysts patterned by EBL varies slightly depending on the desired NW diameter, but the overall principle remains the same. A spincoating process is used to apply an e-beam resist to the sample. Spincoating recipes and the resulting resist thicknesses can be found in Appendix A. These resists are organic polymers that decompose into their constituent monomers when exposed to an electron beam. A Raith 150 Two Direct Write e-beam lithography system is used to expose the pattern of Au catalyst particles. Exposed sections of resist can then be removed using a developing solution leaving well defined holes holes in the resist. When metal is deposited over the entire sample, the remaining resist can be removed leaving metal only in exposed areas.

For the larger NWs (130 nm diameter) presented in this work, a two layer resist consisting of a bottom layer of MMA (Methyl Methacrylate) and a top layer of PMMA (Polymethyl Methacrylate) was used. The advantage of such a bilayer resist structure is that it facilitates the liftoff process due to the undercut produced by the MMA layer (see step 2 in Figure 3.1). However, due to the thickness of the bilayer structure, it is challenging to use for structures that are smaller than 100 nm. For this reason, samples patterned with 77 nm diameter NWs used a single layer ZEP 520-A resist. The ZEP resist family has the advantage of high dose sensitivity allowing for an undercut feature similar to the one formed by a MMA/PMMA bilayer to be formed by back scattered electrons during the exposure step. This allows for the quality of the liftoff to be maintained while using a single-layer resist.

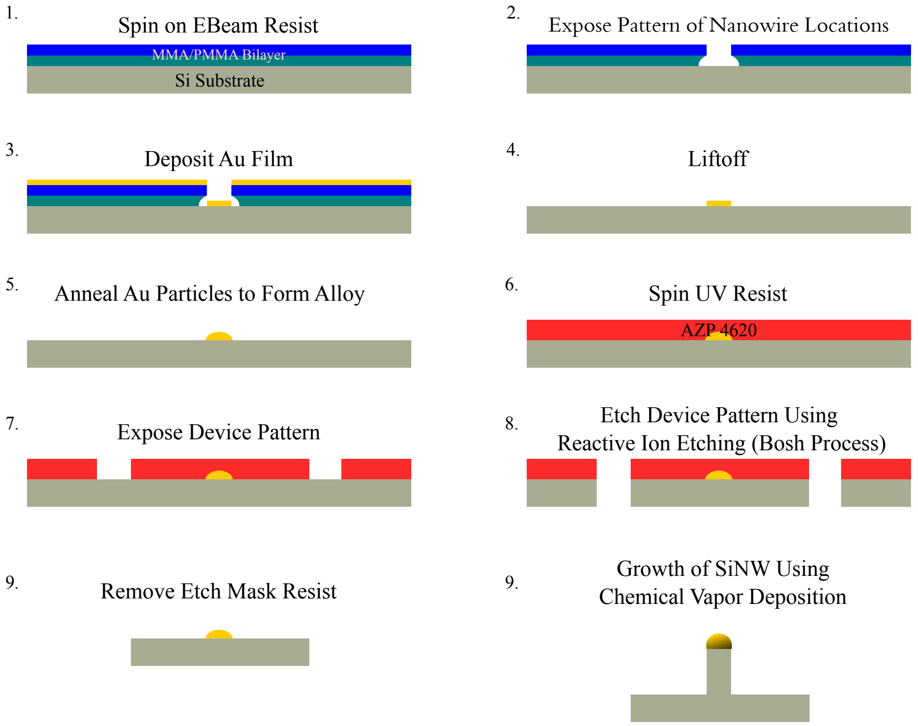

Figure 3.1: Schematic diagram of the SiNW fabrication process.

To expose an area, a series of points is exposed with a step size of 20 nm between each point. The dwell time of the beam is determined by the desired dose (set by the user) and the measured beam current (typically 0.17 nA for a 30 μm aperture and 0.025 nA for a 10 μm aperture). These values along with the step size determine the speed at which the beam is moved across the sample surface, (typically ~ 3 mm/s). The exposed pattern features two sets of catalyst particle arrays as well as three alignment marks to which the etch mask is aligned (Figure 3.3). For the samples discussed in section 5.1, each of these arrays was a single row of dots which will later be located at the edge of a sample chip.

Larger NW samples using MMA/PMMA resist are exposed using a 10 kV electron beam with a 30 μm aperture delivering an area dose of 600 μC/cm^3 and subsequently developed in 1:3 Methyl Isobutyl Ketone (MIBK):IPA for 2 minutes. Samples using ZEP resist are exposed with a 25 kV beam, 10 μm aperture, and an area dose of 520 μC/cm^3 and developed in ZED-N50 (n-Amyl Acetate) for 1.5 minutes. After development, samples are rinsed for 30 seconds in IPA and dried using nitrogen.

Exposed areas are metalized by e-beam evaporation of Au in an Intlvac Nanochrome II evaporator. Prior to loading the sample into the evaporator's vacuum chamber, it is placed in 10-1 buffered oxide etchant for 10 seconds to remove the native oxide layer, ensuring that the deposited Au rests on an oxide-free surface providing a suitable surface for growth to begin to nucleate on. As mentioned above, the oxide etch leaves the surface passivated for approximately 30 minutes [47] so no native oxide layer reforms before the vacuum chamber is evacuated. Au is deposited on the sample surface at a rate of 1 Å/s in an atmosphere of 4×10^{-6} Torr. 52 nm of Au is deposited for the 130 nm NWs and 33 nm is deposited for the 77 nm NWs. Liftoff is done by sonicating the sample in 80°C PG remover for 30 minutes and rinsing in IPA for 1 minute..

Following the liftoff procedure, samples are annealed using an Allwin AccuThermo AW 610 rapid thermal processor (RTP). This system uses high-intensity halogen lamps to heat samples at a rate of up to 50°C/s. Temperature is controlled by measuring the temperature of a carrier wafer using a thermocouple or pyrometer. Samples are heated to 400°C under an Ar flow to prevent surface oxidation and left at temperature for 10 minutes. This process step heats the sample above the eutectic temperature (363°C , Figure 2.5) causing the Au to alloy with the Si substrate. We observed that adding this annealing step to the process significantly improved the yield of vertical NWs, this is attributed to the annealed particle being less susceptible to contamination of the Au-Si interface.

3.2.2 Chip Definition

Due to the requirement that NWs be optically accessible for use as scanning probes, it is essential that they be located as close as possible to the edge of a sample chip. Au catalyst particles cannot be patterned at the edge of a chip because the photoresist at the edge is much thicker than that in the center as a result of the spincoating process, making lithography unreliable if not impossible. To position the Au catalyst particles at the chip edge, we define an area of the wafer to be etched away using deep reactive ion etching (DRIE). The areas to be etched are selected by spincoating the sample in a double-layer AZP 4620 photoresist, exposing the device pattern, and developing the exposed areas to form an etch mask that allows us to etch only the areas where the resist has been removed. The device pattern was exposed using a Heidelberg MLA150 Direct Write UV Lithography system. This system rasters a laser across the sample, switching the beam on and off in order to expose the intended areas. The device pattern is aligned to the deposited Au catalyst particles using a set of three alignment marks that were patterned during the EBL step. For the resist used in this process, samples were exposed using the 405 nm laser with an area dose of 950 mJ/cm^2. Once the exposure is complete, samples are developed in AZ-400K over a period of 4 minutes and rinsed in DI water for 1 minute. The samples are dried with nitrogen and baked at 80°C for 5 minutes in order to remove any remaining moisture from the rinse.

Samples are attached to a 4 inch diameter Si carrier wafer with water-soluble crystal bond adhesive, and loaded into a Oxford Instruments PlasmaLab System 100. Carrier wafers have

5 μm of Si oxide deposited on their surface via plasma-enhanced chemical vapor deposition (PECVD) prior to sample attachment in order to protect them from the etch process.

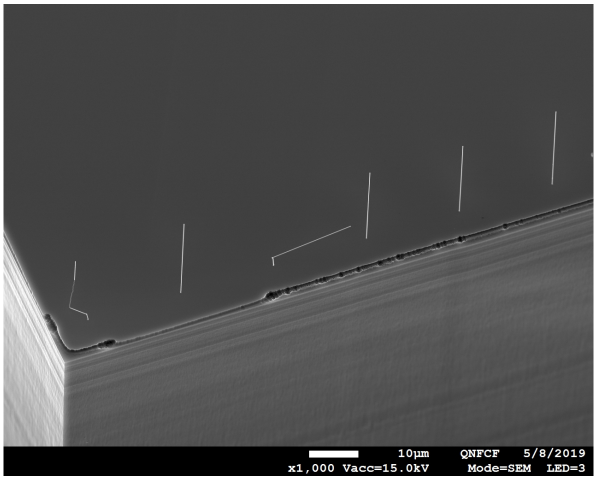

Figure 3.2: SEM image of a section of a SiNW array located 7 μm from the chip edge after DRIE.

For the etch itself, a two-stage etch process known as the Bosch process[48] is used to anisotropically etch the exposed Si. This process alternates between two process modes to achieve a nearly vertical etch, allowing us to define arbitrary device chip geometries. The first etch mode consists of a isotropic plasma etch using sulfur hexafluoride (SF_6). This mode provides the method of material removal. The second mode deposits a passivation layer using Octafluorocyclobutane (C_4F_8). This protective layer resists the etching done in the first mode. Each cycle lasts 12 seconds and 700 cycles are run to completely etch through the sample.

During the etch phase, plasma ions bombard the sample surface directionally from above, causing a sputtering process to occur as they collide with the passivation layer at the bottom of the etch trench. This removes the passivation layer at the bottom of the trench allowing for further etching and keeping the etch nearly perfectly vertical.

Once the etch is completed, the carrier wafer is immersed in 40°C DI water in order to dissolve the crystal bond. The chips are then sonicated in 80°C PG remover for 45 minutes to remove the AZP photoresist.

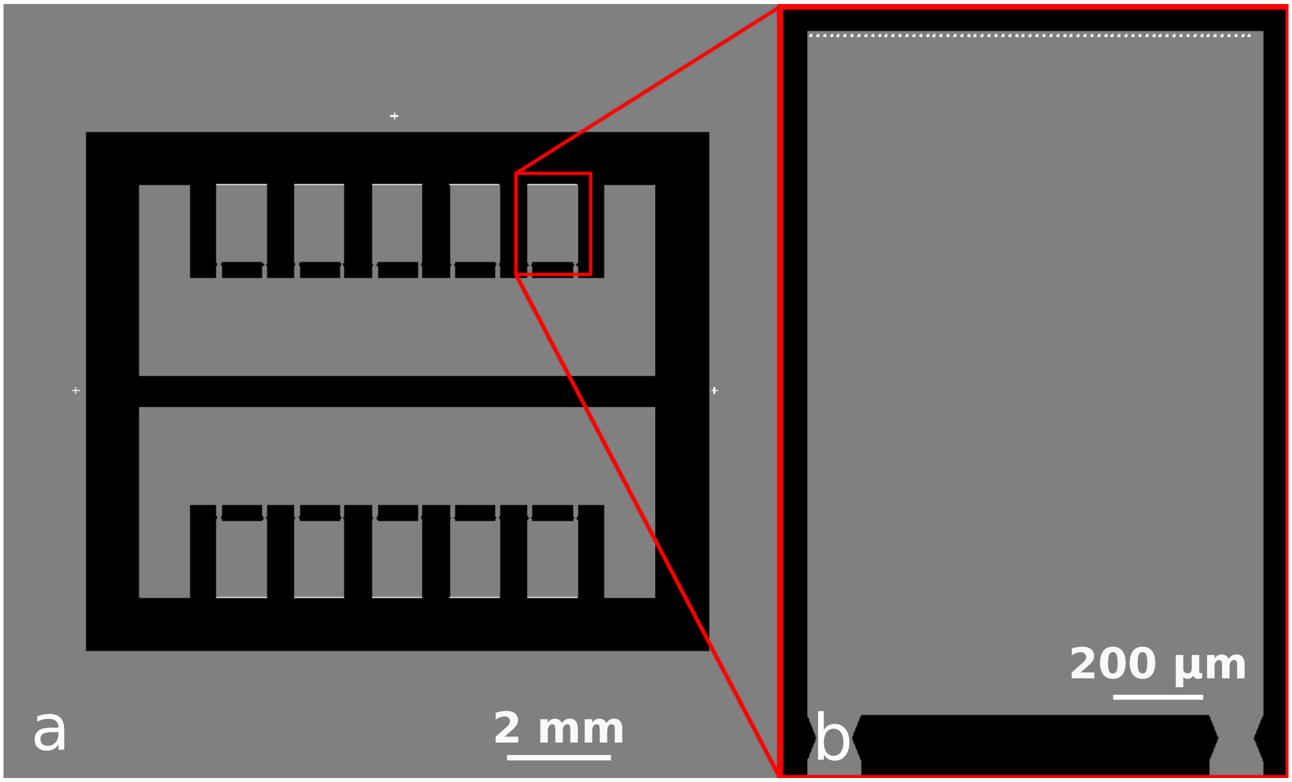

Figure 3.3: Schematic diagram of NW chip EBL and etch patterns. a) Full device pattern. Black areas represent regions removed by DRIE. White crosses and dots represent regions metalized with Au. Crosses are used to align the EBL pattern to the etch mask pattern during UV lithography. b) Zoomed in image of a single NW chip showing position of Au catalyst particles (enlarged for visibility). Tabs at the base of each chip allow single 1 × 1.5 mm chips to be broken out.

3.2.3 Nanowire Growth

Cleaned chips are placed into the load lock of our CVD system and loaded into the process tube where they are left for several hours before the growth process is run. It was found that the quality of grown NWs, as well as the yield of vertical NWs improved for samples left loaded for several hours before growth compared with those grown immediately after loading. This is attributed to the process tube being kept at 100°C while idle. This would remove any moisture that may contaminate the sample before growth.

When the growth recipe begins the process tube is then evacuated to 50 mTorr and backfilled with purified nitrogen to remove any contaminant gases that may be present. The tube is then again evacuated to 50 mTorr before the temperature ramp. A 1 L/min hydrogen flow is introduced to hold the process tube at the process pressure (4 Torr). A variable-speed pump is used in combination with the constant gas flow to control the process pressure. Once the pressure is stabilized, the process tube is ramped to 550°C. When the tube reaches 550°C, the two process gases are introduced: a 10 cm^3/min flow of SiH_4 and a 20 cm^3/min of HCl. Setting the flow rates of these gases relative to the flow rate of H_2 allows for control over the partial pressures of the process gases during growth. With the flow rates listed above, the partial pressures during growth are: $\mathrm{P}_{\mathrm{H}_2} = 3.9$ Torr, $P_{HCl} = 78$ mTorr, and $P_{SiH_4} = 39$ mTorr. The process tube is kept under these conditions for 3 hours for SiNW growth. Since the growth rate is constant with time, the length of the SiNWs can be controlled simply by varying the length of time that process gases are present in the process tube. Once the desired length is reached, the flow of process gases is cut off and the sample is allowed to cool to 300°C under a continued flow of H_2. The tube is then further cooled to 110°C in a flow of N_2 and unloaded from the CVD system.

The flow of SiH_4 provides the Si that is deposited at the base of the catalyst particle. The presence of HCl has been shown to have several beneficial effects on NW growth. NWs grown with HCl exhibit greatly reduced sidewall growth[49] and reduced tapering caused by Au catalyst breakup[50]. Suppression of sidewall growth is essential to growing NWs with a high Q, and preventing catalyst breakup allows us to grow NWs to the 20 µm length in this work[51]. Use of H_2 as a carrier gas has been shown to improve NW quality when compared to inert gases such as He [52] by acting to passivate the Si surface by H-termination of dangling bonds. During the course of this work we attempted several growths using He as a carrier gas and found that significant sidewall growth occurred (Figure 3.4)

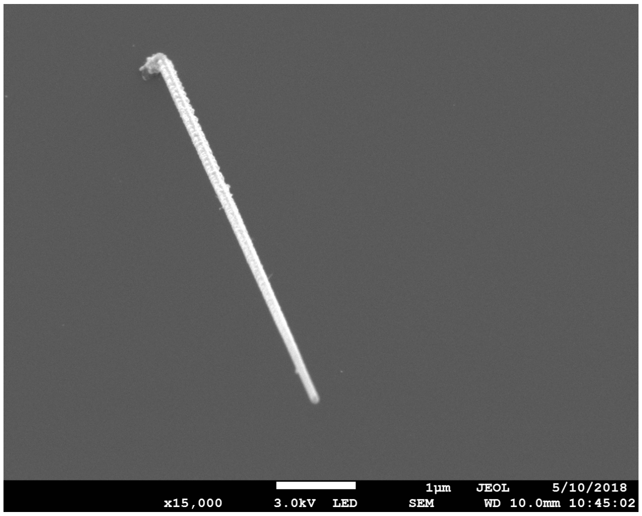

Figure 3.4: SEM image of a SiNW grown with He carrier gas.

3.3 Optimization of Fabrication

In any fabrication process, it ts extremely helpful to ensure that each step is as efficient as possible and achieves the highest possible sample quality. Adding additional process steps or modifying existing ones can dramatically improve sample quality. In this section, the changes that were made to the existing process in order to improve sample quality are described.

After the equipment used for DRIE underwent routine maintenance it we noted a significant reduction in the yield of vertical NWs. SEM imaging revealed microscopic organic contamination on the sample surface due to hardbaking of the etch mask resist due to localized heating caused by the etch process. To remedy this issue, we added an additional SC-1 cleaning step after the DRIE in order to remove this contamination. Since exposing a Si surface to heated H_2O_2 forms an oxide layer several nanometers thick [46], we also added a 1 minute HF step after the SC-1 to ensure that the sample surface is free of oxide before growth. We found that introducing these cleaning steps returned the NW samples to their previous quality.

Originally, the RTP anneal step was placed after the etch process as it was thought that there was little benefit in terms of contamination offered by annealing. Upon reviewing the fabrication process the anneal was moved to immediately following liftoff and a notable increase in vertical yield was observed.

Nanowires were originally grown at 650°C for a much shorter period of time to produce a length of 20 μm. While this yielded a much higher growth rate, the yield of vertical NWs was significantly lower. Upon conducting a literature review, it was determined that growing at a lower temperature would produce a higher yield of vertical NWs. Growths were attempted at 600°C, 625°C, and 550°C. We observed that the yield of vertical NWs was highest at 550°C as was expected. Temperatures lower than 550°C were not explored in detal due to the growth rate decreasing significantly as the temperature is lowered.

Initial flow rates of process gases were 40 cm^3/min of HCl and 20 cm^3/min of SiH_4. When attempting to increase the yield of vertical NWs it was noted that a lower partial pressure of SiH_4 is known to reduce the probability of kinking during growth [41]. Taking this into consideration, flow rates of process gases in the growth recipe was changed to 20 cm^3/min of HCl and 10 cm^3/min of SiH_4. Nearly halving the partial pressure in this way produced growths with noticeably reduced kinking compared to those at higher P_{SiH_4}.

Chapter 4

Measurements

In this chapter the experimental setup used to characterize the mechanical properties of the SiNWs and the measurement process itself are described. Mechanical properties of SiNWs were measured at three temperatures: room temperature (295 K), 77 K, and 4 K. At each of these temperatures, the frequency, and the quality factor were measured for the two fundamental flexural modes. For a perfectly cylindrical beam these two modes would correspond to oscillations in orthogonal directions but with the same frequency. We observe a small frequency splitting between these two modes (typically tens of kHz) which is attributed to a small shape asymmetry in the NW cross section. This results in the two modes being distinguishable from one another in the frequency domain (Figure 4.3).

4.1 Experimental Setup

Thermal motion of the NWs was detected using a 1510 nm optical interferometer. 95% of the output power is sent to a monitor photodiode and the remaining 5% is polarized using a three-paddle polarization controller and sent to the probe. At room temperature, the position of the NW chip was controlled along three axes of motion using a piezo walker motor for the X and Y position and a Picomotor linear actuator for the Z position. These actuators allow for positioning the NW chip with sub-micron accuracy. The interferometer beam can be more finely adjusted using two sets of piezos used for fine X and Y positioning (Figure 4.1). Using these fine adjustment piezos, the interferometer can be scanned over a small region to produce an image of a section of the chip. The position of the beam can then be located anywhere along the length of a single NW in order to maximize the signal intensity.

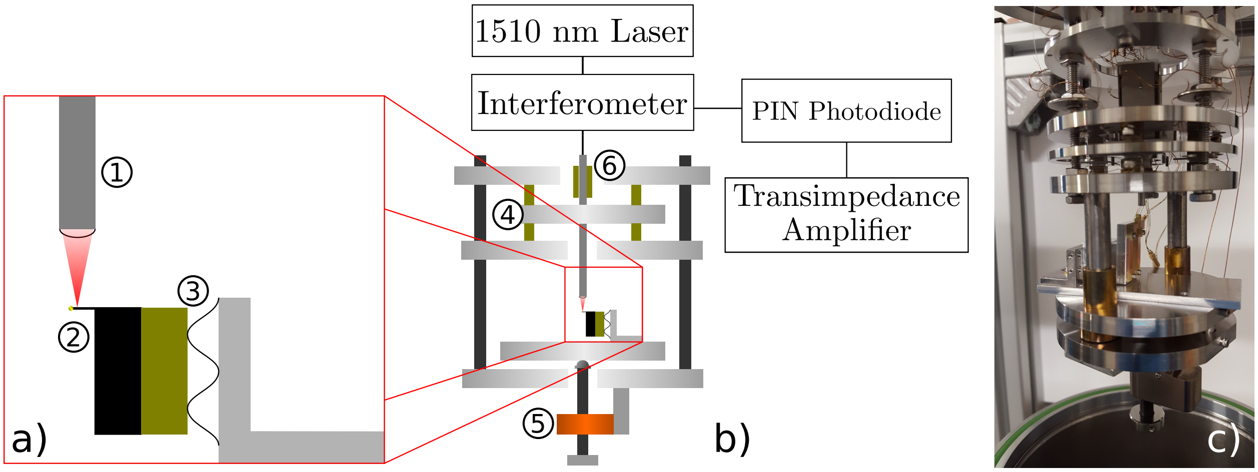

Figure 4.1: Room temperature measurement apparatus. Piezo elements are shown in yellow a,b) Schematic diagram of the measurement apparatus showing: (1) Optical fiber and lens assembly, (2) SiNW chip, (3) Driving piezo and Al foil mount, (4) Piezo walker X/Y position controller, (5) Picomotor Z position controller, (6) Fine adjustment X/Y piezos. c) Photo of room temperature measurement apparatus.

The 1×1.5 mm chip containing the SiNW array was mounted atop a 1×1.5 mm diced shear piezo using Epotek H20E conductive epoxy. This assembly is mounted to a Al foil corrugation which serves to eliminate the mechanical coupling between the driving piezo and the rest of the structure including the NWs. While not used for SiNW characterization, having the ability to drive the NW resonances is useful for experiments envisioned using these NWs.

A Lightpath 355631 lens with a working distance of 280 µm is placed at the end of the interferometer fiber in order to focus the spot size to a 2 µm diameter such that the thermal motion of a single NWs can be detected and measured. The light reflected from the cleaved end of the fiber is interfered with the light reflected off of the NW surface, providing the interference signal. It was discovered in previous work that aligning the polarization of the interferometer beam parallel to the axis of the NW gave a much higher intensity of reflected light [53]. While this is not an issue at room temperature, it is important to consider while taking data at low temperatures to minimize the laser power incident on the NW to prevent heating.

The interferometer signal is detected by an InGaAs PIN photodiode and the resulting photocurrent is amplified and converted to a voltage signal using a FEMTO DHPCA-100 transimpedence amplifier.

NW characterization was also performed at 77 K and 4.2 K in a liquid He cryostat. In this system NW samples are positioned relative to the interferometer beam using Attocube piezoelectric positioners. The optical and fiber positioning setup for these measurements is nearly identical to that used at room temperature. Using this system it is also possible to make measurements of Q and f at room temperature. When this was done, the Qs of each NW sample were found to be higher than those measured in the room temperature setup described above

($9 - 10 \times 10^3$ vs. $11 - 12 \times 10^3$). This is attributed to the vacuum of the room-temperature setup being at a higher pressure than the low-temperature setup, resulting in damping of the NW by residual gas in the system. For the data presented in section 5.1, the values recorded in the cryostat at room temperature are used.

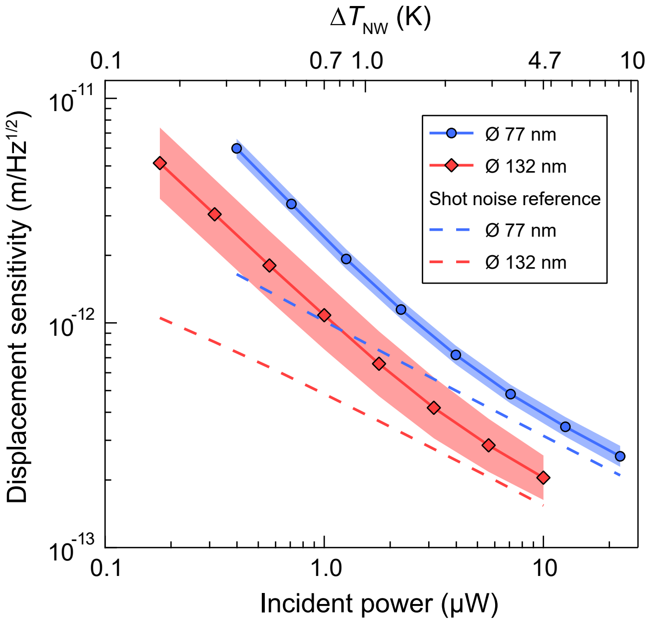

Figure 4.2: Displacement sensitivity vs. incident power for two NWs from each array. Dashed lines indicate the theoretical shot noise limit. Shaded areas indicate the the range of values measured. Change in temperature due to heating is displayed on the top axis. [30] Incident power indicates the power emitted through the lens.

The sensitivity of the interferometer measurement to the displacement of the NW is limited, among other factors, by the laser power applied by the interferometer. At low laser power the noise produced by the amplifier dominates the displacement signal, impairing the ability to detect small displacements. Here, the displacement sensitivity is defined as the displacement spectral density of the voltage noise of the amplified interference signal. This noise arises from two main sources: the photocurrent shot noise and the noise produced by the amplifier electronics. For higher laser powers the displacement sensitivity approaches the shot noise limit; however, the heating of the NW due to optical absorption becomes non-negligible at high incident power leading to higher dissipation. Because of this heating the laser power used during low temperature measurements was 3 μW.

4.2 Measurement Procedure

Once a single NW has been focused on, the interferometer is used to measure the displacement of the NW due to its thermal motion. The current produced by the photodiode $\mathrm{I} = f(x)$ is most sensitive to changes in x, the position of the NW, in the region of maximum $d\mathrm{I}/dx$. Since $f(x)$ is sinusoidal, the region of maximum $d\mathrm{I}/dx$ lies at a point equidistant from a peak and its nearest minimum. This is referred to as being in the center of an interference fringe (Figure 4.3). The Z position of the NW chip is set such that the interferometer signal is at the center of a fringe. Since the displacement of the NW is small, being due only to thermal motion, the signal does not move significantly from the center of the fringe. The power spectral density of the NWs thermal motion is given by the Fourier transform of the AC output of the transimpedence amplifier. Averaging over noise realizations, the PSD of the NW displacement is fitted to the sum of two Lorentzians (Appendix B).

$$S(\omega) = \frac{a_1^2}{(\omega^2 - \omega_1^2)^2 + (\omega^2\omega_1^2/Q_1^2)} + \frac{a_2^2}{(\omega^2 - \omega_2^2)^2 + (\omega^2\omega_2^2/Q_2^2)} \tag{4.1}$$

Where $Q_{1,2}$ are the quality factors, $\omega_{1,2}$ are the resonant frequencies, and $a_{1,2}$ are the rel-

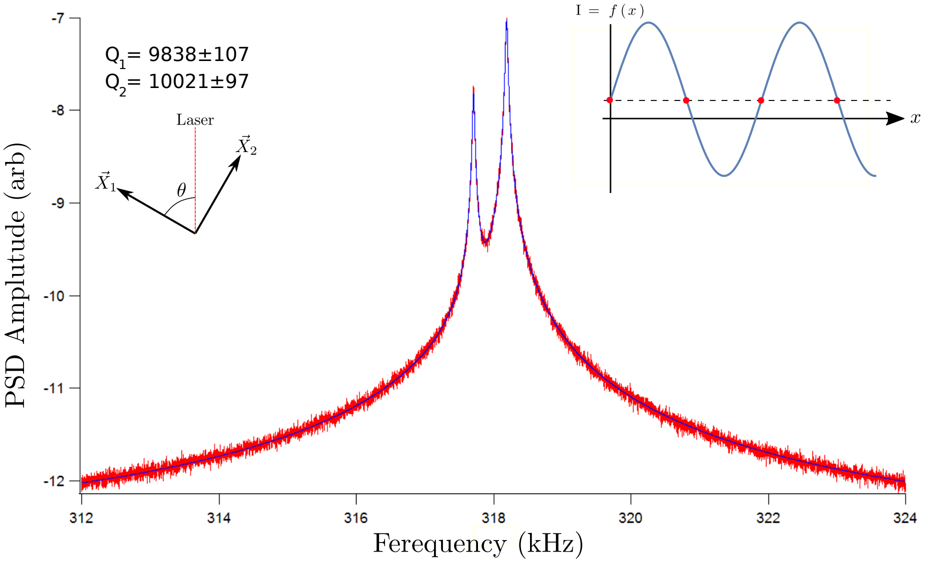

Figure 4.3: Example Power Spectral Density of SiNW oscillation measured at room temperature. Orientation of the two fundamental modes of the NW can be estimated from the relative amplitudes. Measured data is shown in red and the fit to Equation 4.1 is shown in blue. Top right inset shows points at the center of an interference fringe.

ative amplitudes of the fundamental flexural modes. The ratio of a_1/a_2 varies between NWs due to the random orientation of the two modes relative to the interferometer beam.

Using the fit equation, values of ω_1, ω_2, and Q are extracted. For NWs with average diameters of 132 nm and 77 nm, the average frequencies of the fundamental modes are 300 kHz and 170 kHz respectively. Typical Q values are around 11,000 at room temperature. increasing to 55,000 at 4.2 K.

Chapter 5

Results and Conclusion

In this chapter the data for two sets of SiNWs, one consisting of 33 NWs with a 130 nm diameter, and the other consisting of 18 NWs with a 77 nm diameter is presented. For each SiNW in these groups we measured the frequencies of the first two fundamental flexural modes, the quality factor of these resonances, and the spring constants of the NWs using the optical interferomentry technique described in Chapter 4. The measured dimensions of the NWs are used to calculate a theoretical spring constant which is compared to the measured value. The force sensitivity of the NWs fabricated for this work is calculated and compared with singly-clamped sensors presented in other work.

5.1 Data

As described in Equation 2.1, the dissipation of the SiNW cantilever is directly proportional to the NW's spring constant k. While measuring the frequency and Q on a given NW is straightforward using optical interferometry as described in Section 4.2, measuring k is not as simple since the measured value of k is dependent on the position of the focused interferometer beam along the length of the NW. Ideally, focusing the beam at the tip of the NW would allow for an accurate measurement of k, however this is also quite challenging the to the relatively large spot size of the interferometer beam and the difficulty in focusing on the NW tip.

	⌀ (nm)	Δ⌀ (nm)	Length (μm)
Array 1	132 ± 10	4 ± 4	23 ± 1.8
Array 2	77 ± 1	1± 1	23 ± 0.3

Table 5.1: Means and standard deviations of nanowire diameters, difference in base and tip diameters, and lengths measured via SEM.

To provide a more accurate measure of k, we calculate the expected value using Equation 2.2 which depends only on the NW's radius and length. To determine the validity of this method of determining k, the expected frequency value is also calculated using Equation 2.3. The frequency calculated in this way is then compared to the value measured via optical interferometry. A comparison of these values is shown in Table 5.2. For further calculations the measured frequency value is taken to be the correct value.

⌀ (nm)	Calculated f (kHz)	Measured f (kHz)	Error (%)
132 ± 10	291 ± 49	302 ± 54	3.6
77 ± 3	168 ± 8	170 ± 6	1.2

Table 5.2: Mean values and standard deviations of NW diameter (⌀), calculated resonance frequencies, resonance frequencies using optical interferometry, and error between measured and calculated values (calculated as $(f_{meas} - f_{calc})$ / f_{meas}).

It is worth noting that due to the stronger dependence of k on the dimensions of the NW than the dependence on these quantities of f (R^4 vs. R), the error in k may be somewhat larger than the the error in f.

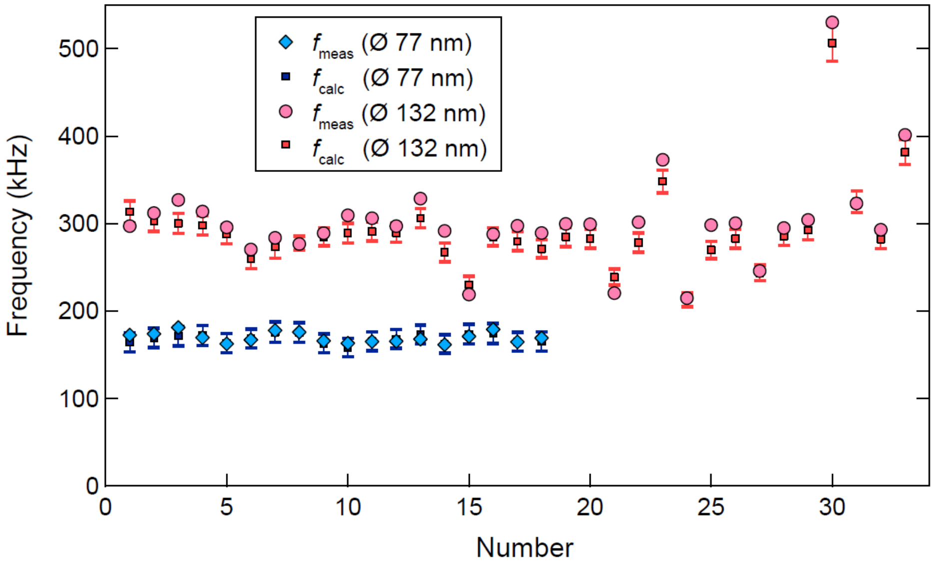

Figure 5.1: Measured and calculated NW frequencies. Values displayed are the average frequency of the two fundamental flexural mode frequencies. [30]

For each NW in both arrays Q and f were measured at room temperature (295 K), 77 K and 4 K. Values of Γ and S_F are calculated for each NW using these values (Table 5.3) using Equations 2.1 and 2.5.

This heating effect was characterized using four NWs, two of each diameter. Heating was measured as a function of optical power and was found to be independent of NW diameter. Although this was not studied in detail, this is attributed to the thermal conductivity of the NW increasing proportionally to the NW's cross-sectional area. This would indicate that the absorbed power is also roughly proportional to cross-sectional area.

To determine the temperature of the NW, the equipartition theorem is used:

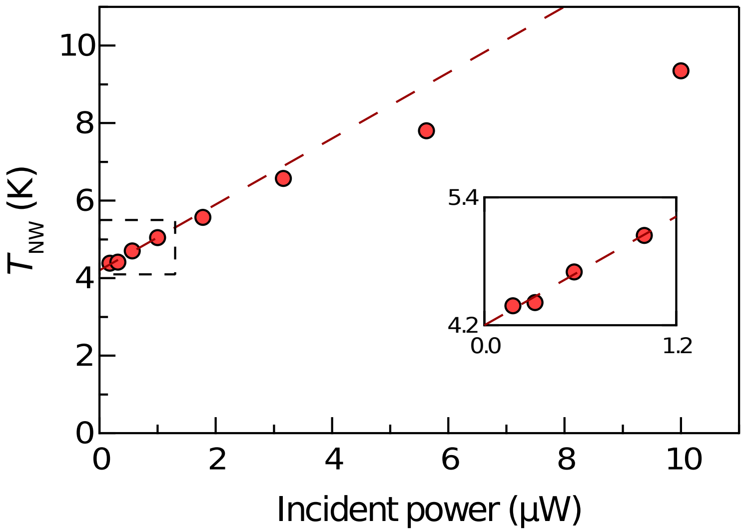

Figure 5.2: SiNW temperature vs. incident laser power for a ⌀132 nm SiNW. Inset shows the data points at the lowest three laser powers used to generate the linear fit. The scale for the temperature axis is set by the point at 4.2 K and 0 µW [30].

$$\frac{1}{2}k_B T = \frac{1}{2}k_n \langle x_n^2 \rangle \tag{5.1}$$

where T is the NW temperature, k_n and $\langle x_n^2 \rangle$ are the spring constant and time-average squared displacement of the n^{th} mode given by integrating over the power spectral density of the measured oscillation of a SiNW (Figure 4.3). The measured displacement is the combined projection of both modes along the the axis of the interferometer beam giving

$$\langle x^2 \rangle = \cos^2(\theta)\langle x_1^2 \rangle + \sin^2(\theta)\langle x_2^2 \rangle. \tag{5.2}$$

It was assumed that since the two modes are nearly degenerate, that $k = k_1 = k_2$ and therefore $k\langle x^2 \rangle = k_B T$.

Similarly to the measurement of k, $\langle x^2 \rangle$ must also be measured at the NW tip, and suffers from the same limitation due to the spot size of the interferometer beam. To avoid this issue, $\langle x^2 \rangle$ is measured at an arbitrary position along the NW and a scaling factor for k is calculated to provide an accurate measurement of temperature. This scaling factor was determined by measuring $\langle x^2 \rangle$ at several low laser powers and assuming that at zero laser power the NW temperature is that of the 4.2 K bath. A linear fit is applied to the lowest three values of $\langle x^2 \rangle$ using the scaling factor for k to calculate the temperature of the NW.

Using this method, we determined that the temperature of the NW was 5.5 K due to an applied laser power of 3 μW.

With the calculated values of S_F, it is possible to estimate what types of forces could be measured using these SiNWs. One of the major research interests of our group is the detection of small ensembles of proton or electron spins. In a magnetic field gradient of 10^6 T/m, a single electron spin would experience a peak force of 9.3 Ån, making a measurement of a single electron spin at cryogenic temperatures achievable using the 77 nm diameter NWs grown in this work. In the same field gradient an ensemble of 51 proton spins would be detectable using the same NW within a 1 Hz bandwidth.

5.2 Comparison With Other Work

In this section, the SiNWs fabricated in this work are compared to other singly-clamped oscillators presented in recent literature. The quantity of interest when making this comparison is the Γ of the oscillator. While some of the literature does present a value of Γ, many sources

T (K)	Measured f (kHz)	Q (10^3)	Γ (10^{-15} kg s^{-1})	$S_F^{1/2}$ (10^{-18} N Hz$^{-1/2}$)
295	302 ± 54 170 ± 6	12 ± 1 11 ± 1	25.8 ± 3.9 5.7 ± 0.5	20.5 ± 1.5 9.7 ± 0.4
77	305 ± 54 171 ± 6	37 ± 4 23 ± 1	8.4 ± 1.3 2.7 ± 0.3	6.0 ± 0.4 3.4 ± 0.2
4.2	305 ± 54 171 ± 6	55 ± 5 55 ± 4	5.8 ± 1.0 1.1± 0.1	1.2 ± 0.1 0.50 ± 0.02

Table 5.3: Mean values and standard deviations of measured frequencies, quality factors, mechanical dissipations, and force noise spectral densities at different bath temperatures. In each row, top values are ⌀132nm NWs and bottom values are ⌀77nm NWs.

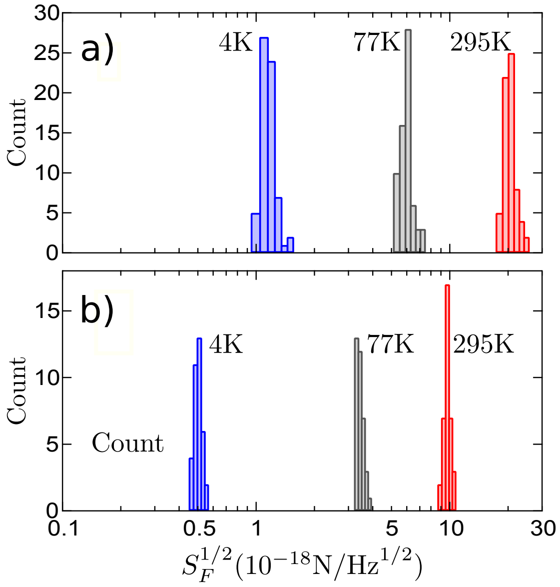

Figure 5.3: Histograms of calculated $S_F^{1/2}$ values from measurements made at room temperature, 77 K and 4 K. a) $S_F^{1/2}$ values for the array of ⌀132 nm NWs. b) $S_F^{1/2}$ values for the array of ⌀77 nm NWs.

do not. For sources that do not directly report a value for Γ, it is calculated using Equation 2.4 from the provided dimensions, materials, and Qs.

As shown in above, the NWs grown for this work have among the lowest dissipation, and

Structure Type	f (kHz)	k (μN/m)	Q (10^3)	Γ (10^{-15} kg s^{-1})	T (K)	Source
Nanowire (Si) $\varnothing$132 nm	302	610	12 55	26 5.8	295 4	This Work
Nanowire (Si) $\varnothing$77 nm	170	68	11 59	5.7 1.1	295 4	This Work
Nanowire (Si) $\varnothing$148 nm	497	380	7	17	295	Nichol *et. al.* [53]
Nanowire (Si) $\varnothing$46 nm	208	28	4	5	295	Nichol *et. al.* [53]
Singly clamped beam (Si)	5	260	86 150	97 55	295 0.11	Mamin *et. al.* [54]
Singly clamped beam (Si)	5	83	11.5 31.5	232 85	295 3	Tao *et. al.* [55]
Singly clamped beam (Diamond)	13	4800	380 800	153 73	295 3	Tao *et. al.* [55]
Nanoladder (Diamond)	25	110	162	3.7	0.14	Héritier *et. al.* [56]
Nanowire (GaAs) $\varnothing$234 nm	581	10500	44.7	64	4	Rossi *et. al.* [25]
Nanowire (GaAs/AlGaAs)	417	-	50	100	4	Rossi *et. al.* [24]
Carbon Nanotube	270	100	250	240	295	Siria *et. al.* [57]

Table 5.4: Comparison with other singly clamped structures reported in literature.

thus the lowest force noise of any singly-clamped oscillators reported in literature. This combined with the ease of optical access obtained by locating these NWs within 10 μm of the chip edge make these very promising probes for a wide range of SPM applications.

5.3 Functionalization

In order to make use of the force sensitivity of these NWs it is necessary to develop methods of functionalizing them for measurement of various forces. Currently envisioned functionnalization schemes typically take the form of attaching a sample to the NW tip which can be accomplished using several techniques depending on the sample. In previous MRFM work NWs were dipped coated in polystyrene in order to measure the statistical polarization of ^{1}H spins [22] and to detect spins in the polystyrene sample to construct a 2D image [23].

Several methods of functionalization are currently being explored using the NWs presented in this work. Attachment of InP NWs to the SiNW tip using Van der Waals forces has been demonstrated and in future work will be used for a proposed experimental realization of atomic resolution NMR diffraction [58]. Preliminary work has been done on depositing magnetic material on the NW tip for use in magnetic force sensing has also been done. 30 nm of 50/50 Fe/Co was deposited on the tips of an array of SiNWs however ensuring that no material is deposited on the NW side walls is essential to avoid reduction of the Q of the NW.

We also envision attaching biomolecules to the NW tip using thiol functionalization to allow for adhesion to the Au catalyst particle [59] for use in MRFM imaging.

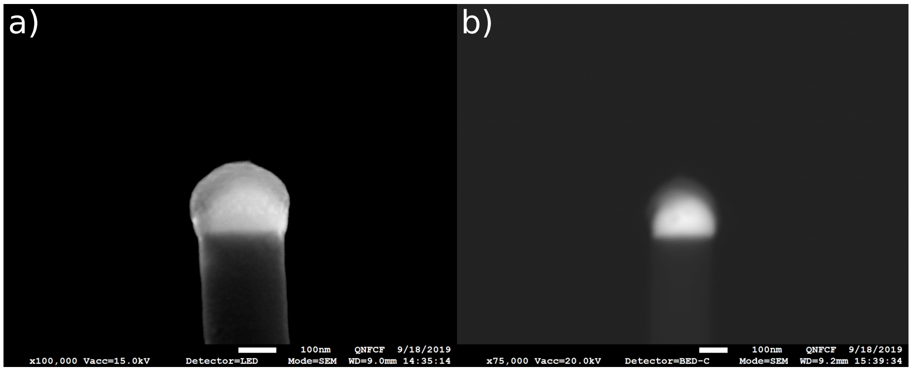

Figure 5.4: a) SEM image of SiNW tip with evaporated 50/50 FeCo film. b) Backscattered electron image of SiNW tip showing the high Z contrast between the deposited FeCo and the Au catalyst particle.

5.4 Conclusion and Future Work

In this thesis, the qualities and properties necessary for ultra-sensitive force detection are described and it is shown that self-assembled silicon nanowire structures are ideal candidates for such applications. A method of fabricating high quality arrays of vertical SiNWs located at the edge of a Si chip is described using lithographic patterning of the Au catalyst particles and deep reactive ion etching to define the device shape. We describe the growth dynamics and procedure, with emphasis on the use of HCl during growth as a method to prevent catalyst breakup, allowing NWs to be grown with high aspect ratio and surface quality. We present a method of characterizing the mechanical properties of grown SiNWs using optical interferometry and provide data obtained from two arrays of SiNWs with different diameters. It is shown that the NW structures grown in this work have, to our knowledge, the lowest mechanical dissipation of any singly-clamped structure reported in literature.

With the ultra-high force sensitivity of the SiNWs presented in this work, one can imagine a host of possible applications that can be explored. It would be interesting to continue to experiment with different methods of functionalizing these NWs for various SPM applications such as vectorial imaging of currents using magnetic-tipped NWs.

It would also be interesting to continue to characterize these NWs at temperatures below 5.5 K, however, doing so would require a method of applying a smaller laser power to reduce heating while still maintaining sufficient signal for detection of the motion of the NWs. It has been suggested that replacing the PIN photodiode used for detection of the interference signal with an avalanche photodiode could be a solution to this.

The arrays of $\varnothing$77 nm NWs suffered from a relatively low vertical yield compared to the larger NWs (18/132 compared to 33/50). This is likely due to the use of the same growth recipe being used for both sizes due to the lack of time to re-optimize the growth parameters for smaller diameter wires. Additionally, many of these NWs that initially appear vertical suffer from kinking near their tips. This is expected to occur for NWs with reduced diameters [41] and can be improved by lowering the SiH_4 partial pressure or increasing the growth temperature. It would be helpful to investigate modifying the growth recipe to improve the yield of these NWs.

References

[1] Paul Girard. Electrostatic force microscopy: principles and some applications to semiconductors. *Nanotechnology*, 12(4):485–490, nov 2001.

[2] D. Rugar, H. J. Mamin, P. Guethner, S. E. Lambert, J. E. Stern, I. McFadyen, and T. Yogi. Magnetic force microscopy: General principles and application to longitudinal recording media. *Journal of Applied Physics*, 68(3):1169–1183, 1990.

[3] D. Rugar, R. Budakian, and H. Mamin. Single spin detection by magnetic resonance force microscopy. *Nature*, 430:329–332, 2004.

[4] C. L. Degen, M. Poggio, H. J. Mamin, C. T. Rettner, and D. Rugar. Nanoscale magnetic resonance imaging. *Proc. Natl. Acad. Sci. U. S. A.*, 106(5):1313–1317, 2009.

[5] Gabriel Vidal-Álvarez, Jordi Agustí, Francesc Torres, Gabriel Abadal, Núria Barniol, Jordi Llobet, Marc Sansa, Marta Fernández-Regúlez, Francesc Pérez-Murano, Álvaro San Paulo, and Oded Gottlieb. Top-down silicon microcantilever with coupled bottom-up silicon nanowire for enhanced mass resolution. *Nanotechnology*, 26(14):145502, mar 2015.

[6] Y. T. Yang, C. Callegari, X. L. Feng, K. L. Ekinci, and M. L. Roukes. Zeptogram-scale nanomechanical mass sensing. *Nano Lett.*, 6(4):583–586, 2006. PMID: 16608248.

[7] G. Binnig, H. Rohrer, Ch. Gerber, and E. Weibel. Surface studies by scanning tunneling microscopy. *Phys. Rev. Lett.*, 49:57–61, Jul 1982.

[8] G. Binnig, C. F. Quate, and Ch. Gerber. Atomic force microscope. *Phys. Rev. Lett.*, 56:930–933, Mar 1986.

[9] Nakamura M. and Yamamda H. *Roadmap of Scanning Probe Microscopy.* Springer Berlin Heidelberg, 2007.

[10] W. Ducker, T. Sneden, and R. Pashley. Direct measurement of colloidal forces using an atomic force microscope. *Nature*, 353:239–241, 1991.

[11] C. Daniel Frisbie, Lawrence F. Rozsnyai, Aleksandr Noy, Mark S. Wrighton, and Charles M. Lieber. Functional group imaging by chemical force microscopy. *Science*, 265(5181):2071–2074, 1994.

[12] Moser J., Güttinger J., and Eichler A. *et. al.* Ultrasensitive force detection with a nanotube mechanical resonator. *Nat. Nano.*, 8:493–496, 2013.

[13] J. Scott Bunch, Arend M. van der Zande, Scott S. Verbridge, Ian W. Frank, David M. Tanenbaum, Jeevak M. Parpia, Harold G. Craighead, and Paul L. McEuen. Electromechanical resonators from graphene sheets. *Science*, 315(5811):490–493, 2007.

[14] F R Braakman and M Poggio. Force sensing with nanowire cantilevers. *Nanotechnology*, 30(33):332001, May 2019.

[15] Z. Huang, H. Fang, and J. Zhu. Fabrication of silicon nanowire arrays with controlled diameter, length, and density. *Advanced Materials*, 19(5):744–748, 2007.

[16] R. S. Wagner and W. C. Ellis. Vapor-liquid-solid mechanism of single crystal growth. *Appl. Phys. Lett.*, 4(89), Febuary 1964.

[17] M. Heurlin, M. Magnusson, D. Lindgren, M. Ek, L. Wallenburg, K. Deppert, and L. Samuelson. Continuous gas-phase synthesis of nanowires with tunable properties. *Nature*, 56:90–94, December 2012.

[18] C. Colombo, D. Spirkoska, M. Frimmer, G. Abstreiter, and A. Fontcuberta i Morral. Ga-assisted catalyst-free growth mechanism of gaas nanowires by molecular beam epitaxy. *Phys. Rev. B*, 77:155326, Apr 2008.

[19] Massimo Mongillo, Panayotis Spathis, Georgios Katsaros, Pascal Gentile, and Silvano De Franceschi. Multifunctional devices and logic gates with undoped silicon nanowires. *Nano. Lett.*, 12(6):3074–3079, 2012.

[20] Peng Yu, Jiang Wu, Shenting Liu, Jie Xiong, Chennupati Jagadish, and Zhiming M. Wang. Design and fabrication of silicon nanowires towards efficient solar cells. *Nano Today*, 11(6):704 – 737, 2016.

[21] R. Yan, D. Gargas, and P. Yang. Nanowire photonics. *Nat. Photonics*, 3:569–5767, 2009.

[22] John M. Nichol, Eric R. Hemesath, Lincoln J. Lauhon, and Raffi Budakian. Nanomechanical detection of nuclear magnetic resonance using a silicon nanowire oscillator. *Phys. Rev. B*, 85:054414, Feb 2012.

[23] John M. Nichol, Tyler R. Naibert, Eric R. Hemesath, Lincoln J. Lauhon, and Raffi Budakian. Nanoscale fourier-transform magnetic resonance imaging. *Phys. Rev. X*, 3:031016, Sep 2013.

[24] Nicola Rossi, Floris R. Braakman, Davide Cadeddu, Denis Vasyukov, Gözde Tütüncüoglu, Anna Fontcuberta i Morral, and Martino Poggio. Vectorial scanning force microscopy using a nanowire sensor. *Nat. Nanotechnol.*, 12:150–155, 2016.

[25] N. Rossi, B. Gross, F. Dirnberger, D. Bougeard, and M. Poggio. Magnetic force sensing using a self-assembled nanowire. *Nano Lett.*, 19(2):930–936, 2019.

[26] A. Gloppe, P. Verlot, E. Dupont-Ferrier, A. Siria, P. Poncharal, G. Bachelier, P. Vincent, and O. Arcizet. Bidimensional nano-optomechanics and topological backaction in a non-conservative radiation force field. *Nat. Nano.*, 9:920–926, 2014.

[27] J. A. Sidles, J. L. Garbini, K. J. Bruland, D. Rugar, O. Züger, S. Hoen, and C. S. Yannoni. Magnetic resonance force microscopy. *Rev. Mod. Phys.*, 67:249–265, Jan 1995.

[28] K. Y. Yasumura, T. D. Stowe, E. M. Chow, T. Pfafman, T. W. Kenny, B. C. Stipe, and D. Rugar. Quality factors in micron- and submicron-thick cantilevers. *J. Microelectromech. Syst.*, 9(1):117–125, March 2000.

[29] Y Tao, P Navaretti, R Hauert, U Grob, M Poggio, and C L Degen. Permanent reduction of dissipation in nanomechanical si resonators by chemical surface protection. *Nanotechnology*, 26(46):465501, oct 2015.

[30] Pardis Sahafi, William Rose, Andrew Jordan, Ben Yager, Michèle Piscitelli, and Raffi Budakian. Ultra-low dissipation patterned silicon nanowire arrays for scanning probe microscopy. *Nano Lett.*, November 2019.

[31] Fateen Zafar and Azhar Iqbal. Indium phosphide nanowires and their applications in optoelectronic devices. *Proc. R. Soc.*, 472, 2016.

[32] Young-Soo Sohn, Jinsung Park, Gwonchan Yoon, Jiseok Song, Sang-Won Jee, Jung-Ho Lee, Sungsoo Na, Taeyun Kwon, and Kilho Eom. Mechanical properties of silicon nanowires. *Nanoscale Res. Lett.*, 5(211), 2009.

[33] Mikhail Dunaevskiy, Pavel Geydt, Erkki Lähderanta, Prokhor Alekseev, Tuomas Haggrén, Joona-Pekko Kakko, Hua Jiang, and Harri Lipsanen. Young's modulus of wurtzite and zinc blende inp nanowires. *Nano Lett.*, 17(6):3441–3446, 2017. PMID: 28534623.

[34] Vladimir Dubrovskii. *Nucleation Theory and Growth of Nanostructures*. Springer, January 2014.

[35] Volker Schmidt, Joerg V. Wittemann, Stephan Senz, and Ulrich Gösele. Silicon nanowires: A review on aspects of their growth and their electrical properties. *Advanced Materials*, 21(25-26):2681–2702, 2009.

[36] V. Schmidt, J. Wittemann, and U. Gosele. Growth, thermodynamics, and electrical properties of silicon nanowires. *Chem. Rev.*, 30(33):332001, 2010.

[37] V. A. Nebol'sin and A. A. Shchetinin. Role of surface energy in the vapor–liquid–solid growth of silicon. *Inorganic Materials*, 39(9):899–903, Sep 2003.

[38] C.-Y. Wen, M. C. Reuter, J. Tersoff, E. A. Stach, and F. M. Ross. Structure, growth kinetics, and ledge flow during vaporsolidsolid growth of copper-catalyzed silicon nanowires. *Nano Lett.*, 10(2):514–519, 2010. PMID: 20041666.

[39] Joerg V. Wittemann, Wolfram Münchgesang, Stephan Senz, and Volker Schmidt. Silver catalyzed ultrathin silicon nanowires grown by low-temperature chemical-vapor-deposition. *Journal of Applied Physics*, 107(9):096105, 2010.

[40] X. Li, J. Ni, and R. Zhang. A thermodynamic model of diameter- and temperature-dependent semiconductor nanowire growth. *Sci. Rep.*, 7:15029, 2017.

[41] J. Westwater, D. P. Gosain, S. Tomiya, S. Usui, and H. Ruda. Growth of silicon nanowires via gold/silane vapor–liquid–solid reaction. *Journal of Vacuum Science & Technology B*, 15(3):554–557, 1997.

[42] H. Okamoto and T. Massalski. *Binary Alloy Phase Diagrams Vol. 1*. ASM International, September 1983.

[43] Ludger Overmeyer, Yixiao Wang, and Tim Wolfer. *Eutectic Bonding*, pages 488–492. Springer Berlin Heidelberg, Berlin, Heidelberg, 2014.

[44] S. Kodambaka, J. Tersoff, M. C. Reuter, and F. M. Ross. Diameter-independent kinetics in the vapor-liquid-solid growth of si nanowires. *Phys. Rev. Lett.*, 96:096105, Mar 2006.

[45] B. Ressel, K. C. Prince, S. Heun, and Y. Homma. Wetting of si surfaces by au–si liquid alloys. *Journal of Applied Physics*, 93(7):3886–3892, 2003.

[46] UC Irvine. Cleaning procedures for silicon wafers. Technical report, UC Irvine.

[47] L.E. Black, B.W.H. van de Loo, B. Macco, J. Melskens, W.J.H. Berghuis, and W.M.M. Kessels. Explorative studies of novel silicon surface passivation materials: Considerations and lessons learned. *Solar Energy Materials and Solar Cells*, 188:182 – 189, 2018.

[48] F. Laermer. Method of anisotropically etching silicon. (5501893), March 1996.

[49] F Oehler, P Gentile, T Baron, and P Ferret. The effects of hcl on silicon nanowire growth: surface chlorination and existence of a 'diffusion-limited minimum diameter'. *Nanotechnology*, 20:475307, 2009.

[50] P Gentile, A Solanki, N Pauc, F Oehler, B Salem, G Rosaz, T Baron, M Den Hertog, and V Calvo. Effect of hcl on the doping and shape control of silicon nanowires. *Nanotechnology*, 23:215702, 2012.

[51] J. B. Hannon, S. Kodambaka, F. M. Ross, and R. M. Tromp. The influence of the surface migration of gold on the growth of silicon nanowires. *Nature*, 440:69, 2006.

[52] Y. Wu, Y. Cui, L. Huynh, C. Barrelet, D. Bell, and C. Lieber. Controlled growth and structures of molecular-scale silicon nanowires. *Nano. Lett.*, 4(3):433–436, 2004.

[53] J. Nichol, E. Hemesath, L. Lauhon, and R. Budakian. Displacement detection of silicon nanowires by polarization-enhanced fiberoptic interferometry. *Appl. Phys. Lett.*, page 193110, 2008.

[54] H. J. Mamin and D. Rugar. Sub-attonewton force detection at millikelvin temperatures. *Appl. Phys. Lett.*, 79(20):3358–3360, 2001.

[55] Y. Tao, J. Boss, B Moores, and C. Degen. Single-crystal diamond nanomechanical resonators with quality factors exceeding one million. *Nat. Commun.*, 5(3638), 2014.

[56] M. Héritier, A. Eichler, Y. Pan, U. Grob, I. Shorubalko, M. D. Krass, Y. Tao, and C. L. Degen. Nanoladder cantilevers made from diamond and silicon. *Nano Lett.*, 18(3):1814–1818, 2018. PMID: 29412676.

[57] A. Siria and A. Niguès. Single-crystal diamond nanomechanical resonators with quality factors exceeding one million. *Sci. Rep.*, 7(11595), 2017.

[58] P Mansfield and P K Grannell. NMR 'diffraction' in solids? *Journal of Physics C: Solid State Physics*, 6(22):L422–L426, nov 1973.

[59] Y. Xue, X. Li, H. Li, and W Zhang. Quantifying thiol gold interactions towards the efficient strength control. *Nat. Commun.*, 5(4348), 2014.

Appendices

Appendix A

Spincoating Recipes

Spincoating recipes typically follow a standard ramp profile consisting of a slow ramp to a relatively low speed (typically around 500 rpm) which is held for several seconds to spread the resist out over the sample surface followed by a faster ramp to a high speed (typically around 5000 rpm) to thin the resist out to the desired thickness.

Prior to each spin recipe, samples are heated to >100°C for 5 minutes as a dehydration bake to remove any moisture on their surface, improving resist adhesion. Once the bake is complete, samples are placed on a vacuum chuck and several drops of resist are applied until the sample is completely covered. The sample is then spun following the appropriate spincoating recipe.

Recipe for MMA EL10/PMMA A3 Bilayer

Step Number	Speed (rpm)	Ramp Rate (rpm/s)	Time (s)
1	500	200	1.3
2	4000	1000	24.5
3	0	1000	0

Table A.1: MMA Spincoating recipe

After the MMA layer is spun, the resist is baked by heating the sample to 150°Cfor 3 minutes on a hotplate. Following this step the sample is placed back on the vacuum chuck and PMMA is applied and spun.

Step Number	Speed (rpm)	Ramp Rate (rpm/s)	Time (s)
1	500	200	1.3
2	5000	1000	24.5
3	0	1000	0

Table A.2: PMMA spincoating recipe

The sample is then placed on a hotplate at 180°C to bake the PMMA layer. This process produces a double-layer MMA/PMMA resist with a total thickness of approximately 650 nm.

Recipe for ZEP 520-A Ebeam resist

Step Number	Speed (rpm)	Ramp Rate (rpm/s)	Time (s)
1	6000	1000	60
2	0	1000	0

Table A.3: ZEP 520-A spincoating recipe

After the ZEP layer is spun, it is baked at 180 °C for 3 minutes. Following this process yields a single-layer ZEP resist with a thickness of 300 nm

Recipe for AZP 4620 Photoresist

Step Number	Speed (rpm)	Ramp Rate (rpm/s)	Time (s)
1	300	100	3
2	2500	500	60
3	0	500	0

Table A.4: AZP 4620 spincoating recipe 1

Once the first layer of AZP 4620 is applied, it is baked at 110°C for 3 minutes. The sample is then returned to the spincoater and a second layer of resist is applied using recipe 2. This second layer serves to increase the thickness of the resist, allowing it to better withstand the long DRIE process.

Step Number	Speed (rpm)	Ramp Rate (rpm/s)	Time (s)
1	300	100	3
2	1600	500	60
3	0	500	0

Table A.5: AZP 4620 spincoating recipe 2

After the second layer is spun the sample is returned to the 110°C hotplate for 2 minutes 45 seconds. This recipe produces a double-layer AZP 4620 resist with a total thickness of 21 μm.

Appendix B

Power Spectral Density of Thermal Displacement for a Harmonic Oscillator

To determine the appropriate fit function for the Fourier transformed interferometer signal, we model the NW as a damped harmonic oscillator with center frequency ω_0 and quality factor Q, as well as a stochastic drive due to its thermal motion. For such an oscillator, the equation of motion is

$$\eta(t) = \omega_0^2 x(t) + \frac{\omega_0}{Q}\dot{x}(t) + \ddot{x}(t) \tag{B.1}$$

where $\eta(t)$ is a stationary random process with $\langle \eta(t) \rangle = 0$. Taking the Fourier transform of both sides for a particular realization of $\eta(t)$

$$\left(-\omega^2 - i\frac{\omega\omega_0}{Q} + \omega_0^2\right)\tilde{x}(\omega) = \tilde{\eta}(\omega) \tag{B.2}$$

Solving for $\tilde{x}(\omega)$,

$$\tilde{x}(\omega) = \frac{\tilde{\eta}(\omega)}{(\omega_0^2 - \omega^2) - i\frac{\omega\omega_0}{Q}} \tag{B.3}$$

for which the PSD is

$$\begin{aligned} S_x(\omega) &= \langle |x(\omega)^2| \rangle \\ &= \frac{\langle |\eta(\omega)^2| \rangle}{(\omega_0^2 - \omega^2)^2 + \frac{\omega^2\omega_0^2}{Q^2}} \\ &= \frac{S_\eta(\omega)}{(\omega_0^2 - \omega^2)^2 + \frac{\omega^2\omega_0^2}{Q^2}} \end{aligned} \tag{B.4}$$

Assuming η to me a white noise process with $S_\eta(\omega) = \eta_0$,

$$S_x(\omega) = \frac{\eta_0}{(\omega_0^2 - \omega^2)^2 + \frac{\omega^2\omega_0^2}{Q^2}} \tag{B.5}$$

which is a Lorentzian. The generalization to a 2D harmonic oscillator simply results in the addition of another Lorentzian term.